Journal of Alloys and Compounds 509 (2011) 1800–1808

Contents lists available at ScienceDirect

Journal of Alloys and Compounds

journal homepage: www.elsevier.com/locate/jallcom

Origin of giant dielectric constant in $Ba[(Fe_{1-x}Co_x)_{1/2}Nb_{1/2}]O_3$

Devang D. Shah[a,1], P.K. Mehta[a,2], M.S. Desai[b], C.J. Panchal[b,*]

[a] Department of Physics, Faculty of Science, The M.S. University of Baroda, Vadodara-390002, Gujarat, India
[b] Applied Physics Department, Faculty of Technology & Engineering, The M.S. University of Baroda, Vadodara-390001, Gujarat, India

ARTICLE INFO

Article history:
Received 8 July 2010
Received in revised form 4 October 2010
Accepted 13 October 2010
Available online 13 November 2010

Keywords:
Dielectric relaxation
Dielectric constant
Impedance spectroscopy
Transport properties

ABSTRACT

The X-ray diffraction Rietveld refinement of $Ba[(Fe_{1-x}Co_x)_{1/2}Nb_{1/2}]O_3$ with $0 \leq X \leq 1$ shows cubic structure formation with space group P_m3_m. No distinct tilting of oxygen octahedron is observed. The dielectric measurement of such a cubic system exhibited giant values ($\varepsilon' > 10^4$) in the temperature range of 298–483 K and frequency range of 10^2–10^5 Hz. An analysis of the permittivity, electric modulus, and electrical conductivity properties in these systems confirmed the presence of oxygen vacancies induced dipolar relaxation. Our investigations show that the observed extremely high dielectric constant values are predominantly the result of oxygen vacancies induced dipoles produced at the grain boundaries. Additional significant intrinsic contributions to the permittivity comes from the directly doped electrons at the unit cell, as indicated by the enhancement in the observed values of the permittivity on replacement of Fe^{3+} ($3d^5$) by Co^{3+} ($3d^6$). The contributions of the doped free charges and the oxygen vacancy induced dipoles are separated using the Jump Relaxation Model.

1. Introduction

Ceramic compounds exhibiting high dielectric constant ($\varepsilon' > 10^4$) are of enormous importance to the electronic industry due to their wide applications as industrial capacitors, sensors, actuators, power transmission devices, memory devices, high energy storage devices, etc. [1,2]. Several attempts have been made earlier to explain the high dielectric constant in $Pb(Fe_{1/2}Nb_{1/2})O_3$ (PFN), $Pb(Fe_{1/2}Ta_{1/2})O_3$ (PFT), $Pb(Mg_{1/3}Nb_{2/3})O_3$ (PMN), $Ba(Fe_{1/2}Nb_{1/2})O_3$ (BFN), $Sr(Fe_{1/2}Nb_{1/2})O_3$ (SFN), $Pb(Mg_{1/3}Nb_{2/3})O_3$-$PbTiO_3$ (PMN-PT), $Pb(Fe_{1/2}Nb_{1/2})O_3$-$PbTiO_3$ (PFN-PT), $Ba(Fe_{1/2}Nb_{1/2})O_3$-$BaTiO_3$ (BFN-BT), etc. on the basis of chemical disorder leading to a local permanent polarization induced ferroelectricity [1–13]. Alternatively, the high dielectric constant in $CaCu_3Ti_4O_{12}$ (CCTO) like compounds was linked to the extrinsic factors like the grain boundary effects, oxygen vacancies, space charge polarization, etc. [12–20]. It is indeed desirable to have a proper understanding of the origin of the physico-chemical behaviour in these systems for tailoring their appropriate industrial applications. The high dielectric constant of the BFN compound was reported first by Saha and Sinha [7,8]. According to their work, BFN is a relaxor ferroelectric having a monoclinic crystal structure. The same compound was reported as a non-ferroelectric having a cubic crystal structure by Raevski et al. [14] and Wang et al. [15]. Raevski et al. have explained the high dielectric constant for such a cubic system by using the Maxwell–Wagner Effect [14]. Latter on, Wang et al. [15] had explained it in terms of oxygen vacancy induced dielectric relaxation. Most of the previous studies were concentrated on either explaining such high dielectric constant values in individual systems by probing the role of only the extrinsic factors like grain and grain boundary or investigating ferroelectricity with the variation of chemical composition. Looking at the above contradicting explanations for the origin of the high dielectric constant, correlated investigations of the extrinsic as well as the intrinsic contributions of chemical distortion is crucial for a deeper understanding and optimization of the dielectric parameters.

In the present work, the origin of the high dielectric constant, in cubic ABO_3 type defect perovskites is analyzed through a correlated study of the crystal structure, the microstructure, the dielectric relaxation, and the electrical conductivity. The system we chose is $Ba(Fe_{1/2}Nb_{1/2})O_3$ (BFN) compound with substitution of Co at Fe site by 50% and 100%. The selection of Co is essentially made for three different reasons: (1) Fe and Co both having nearly identical ionic radii and thus leads to nearly same tolerance factor, enables us to presume that no significant structural distortion occurs; (2) Fe and Co both having same 3+ valence with one additional electron in the outermost orbital of Co., i.e., Fe^{3+} ($3d^5$) and Co^{3+} ($3d^6$); (3) Co^{3+} ($3d^6$) is having six electrons in the outer orbital, which shows a weak John–Teller Effect [21]. Attempts are made to explain the role of oxygen vacancy as well as the cobalt doping induced dielectric relaxation. Further, we have explained the nature of the ac con-

* Corresponding author. Tel.: +91 9825094761; fax: +91 2652423898.
E-mail addresses: devangshah_04@yahoo.co.in (D.D. Shah), pkmehta_phy@yahoo.co.in (P.K. Mehta), cjpanchal_msu@yahoo.com (C.J. Panchal).
[1] Tel.: +91 9427852073.
[2] Tel.: +91 9377704333.

0925-8388/$ – see front matter © 2010 Elsevier B.V. All rights reserved.
doi:10.1016/j.jallcom.2010.10.045

ductivity using frequency exponent '*s*' as a function of frequency through the Jump Relaxation Model (JRM). The role of the conduction mechanism of charge carriers is also analyzed to explain the origin of high dielectric constant.

2. Experimental

Samples of $BaFe_{1/2}Nb_{1/2}O_3$ (BFN), $BaFe_{1/4}Co_{1/4}Nb_{1/2}O_3$ (BFCN), and $BaCo_{1/2}Nb_{1/2}O_3$ (BCN) were prepared by the conventional solid-state reaction technique. High purity oxides (≥99.99%) of $BaCO_3$, Nb_2O_5, Fe_2O_3, and Co_3O_4 were mixed in stoichiometric quantity. Wet mixing was carried out with acetone as the medium for homogeneous mixing. Grinding was performed using pestle and mortar for about 2 h. Well-mixed powders were calcined at 1400–1500 K for 6 h. The as-calcined powders were compacted into circular disks of 12 mm diameter and 0.5–1.5 mm thickness with an applied pressure of 10 tons. Such pellets were sintered in air at 1400–1500 K for 10 h. X-ray diffraction (XRD) was performed using SHIMADZU-XRD-6000. The Cu Kα radiation with $\theta - 2\theta$ geometry was used to collect the XRD data. The scanning was performed from $2\theta = 10$–110° with a step of 0.02° and a scanning rate of 1.0°/min. The microstructure photographs of the samples were collected using a scanning electron microscope (SEM). The SEM photographs were collected for three different regions for each sample to ensure the correctness of the results. For electrical characterization, pellets were first polished and then electrodes were made using silver paste. Impedance data were collected at different temperatures, with an interval of 5 K, using a Solatron-1260 Impedance Analyzer in the frequency range of 10^0–10^7 Hz. The temperature was increased from 298 K to 483 K, at a constant heating rate of 0.5 K/min. The collected impedance data were converted into permittivity and conductivity data using appropriate sample dimensions.

3. Results and discussions

3.1. Structural analysis

Powder-XRD patterns of BFN, BFCN, and BCN compounds, along with their Rietveld refinement profiles, are shown in Fig. 1. All samples show a single cubic phase formation with space group P_m3_m. The refined cell parameters for BFN, BFCN, and BCN are $a = 4.0573$ Å, $a = 4.0714$ Å, and $a = 4.0843$ Å, respectively. The lattice parameters obtained through the Rietveld refinement indicate systematic lattice expansion on gradual replacement of Fe^{3+} by Co^{3+}. The observed expansion in unit cell is due to the removal of degeneracy in unevenly filled t_{2g} levels of O2p–Co3d^6 in comparison with the degenerate O2p–Fe3d^5 levels leading to a weak John–Teller Effect [21]. The delocalization of the orbital leads to a softening of the overlap, which in turn leads to the expansion of unit cell. Further, contrary to other modified ABO_3 systems [3,4,6,7], no significant in-plane or out-of-plane tilting of the oxygen octahedron is observed in the present system. The goodness parameter of Rietveld refinement ($S \sim 1.26$), as well as, the calculated percentage densification (more than 84%), indicate that the samples are of good quality.

The microstructure photographs taken using SEM are shown in Fig. 2. A uniform grain formation is observed for each sample. The observed average grain size of BFN, BFCN, and BCN are ~10 μm, ~5 μm and ~1 μm, respectively. Though synthesis cycle for each of these compositions were optimized for highest densification, the gradual reduction in grain size with Co substitution can not directly inferred to any single reason. A grain size of the order of ~0.5 μm for BCN compound prepared through solid state reaction technique was reported by Lu et al. [22].

3.2. Dielectric relaxation analysis

The frequency response of the real permittivity data (dielectric constant), $\varepsilon'(f)$, at various temperatures, is shown in Fig. 3. The values of the real permittivity are very high (~10^4) for each of these samples. This is in contradiction to the general observation that the dielectric constants for cubic structures must be very small. Under this condition, the observed high dielectric constant points to a significant contribution of the extrinsic factors only. In this

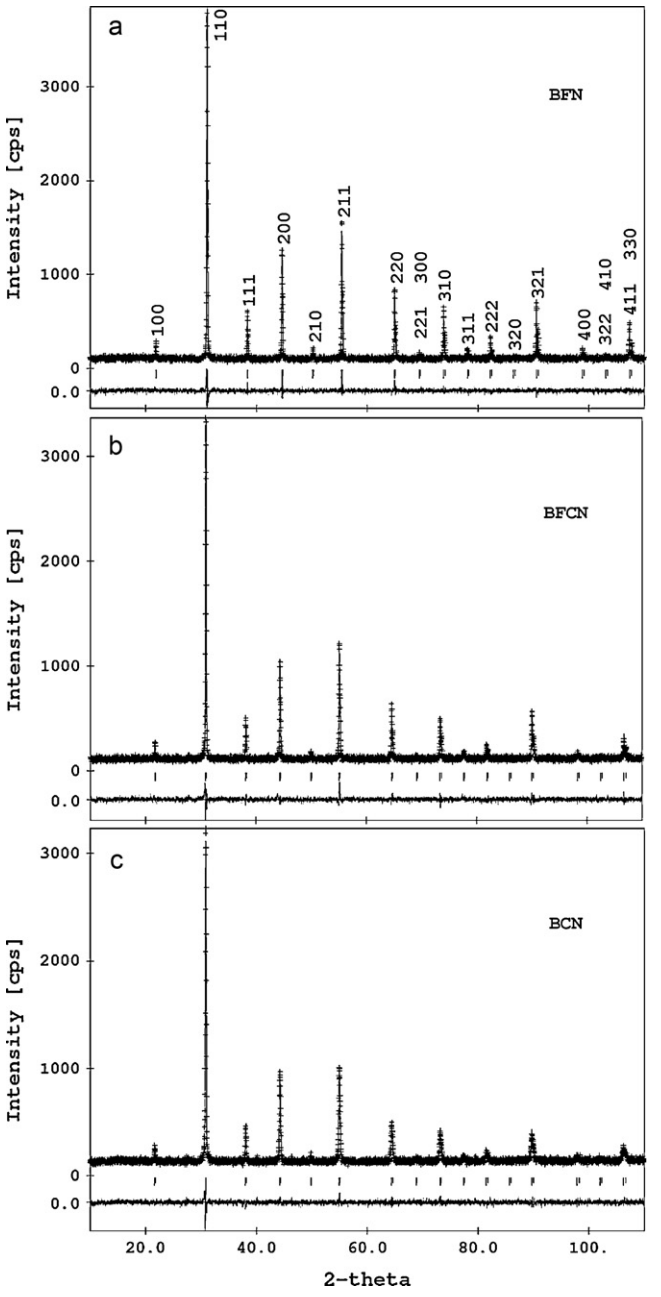

Fig. 1. The observed (+ sign), calculated (continuous line), and difference (bottom line) profiles obtained after the Rietveld refinement of: (a) BFN, (b) BFCN, and (c) BCN. The vertical bars denote the position of the Bragg reflection. The corresponding sets of ($h\,k\,l$) planes are shown.

regard, according to the Maxwell–Wagner theory of extrinsic factors, the dielectric constant is directly proportional to the grain size of the samples. In contrast to the above theory, we observed that the BCN sample having the smallest grain size (Fig. 2(c)), shows highest dielectric constant (~10,000 at 298 K, 1 kHz). On the other hand, BFN having the largest grain size (Fig. 2(a)), shows lowest dielectric constant (~2000 at 298 K, 1 kHz) among them. A comparison of the real permittivity data in the above samples shows that the overall dielectric constant values increases with increase in the concentration of Co. The reason for the high dielectric constant therefore is not just the grain-boundary and the grain-size dependent extrinsic factors, but a significant contribution of the intrinsic factors related to chemical substitution induced localized electronic structure modifications also play a crucial role.

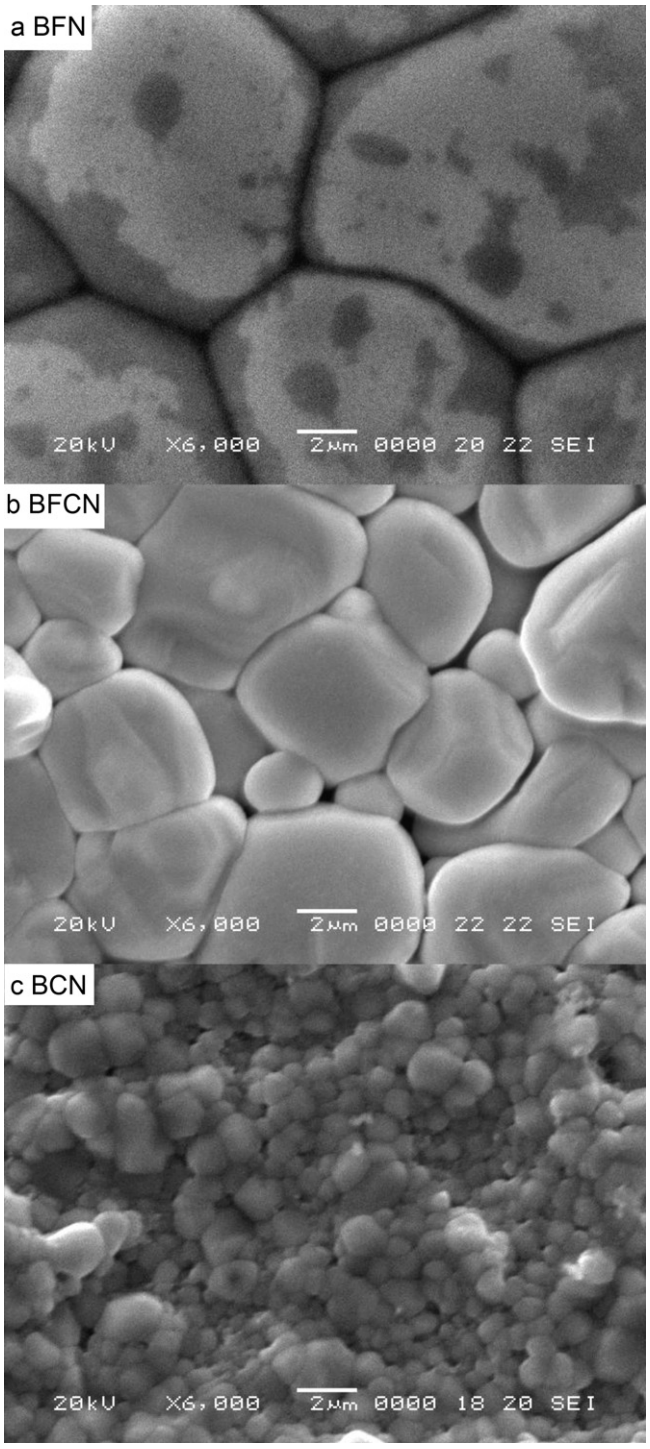

Fig. 2. The microstructure images of: (a) BFN, (b) BFCN, and (c) BCN obtained using scanning electron microscopy (SEM). The magnification is kept same at ×6000 times for all images.

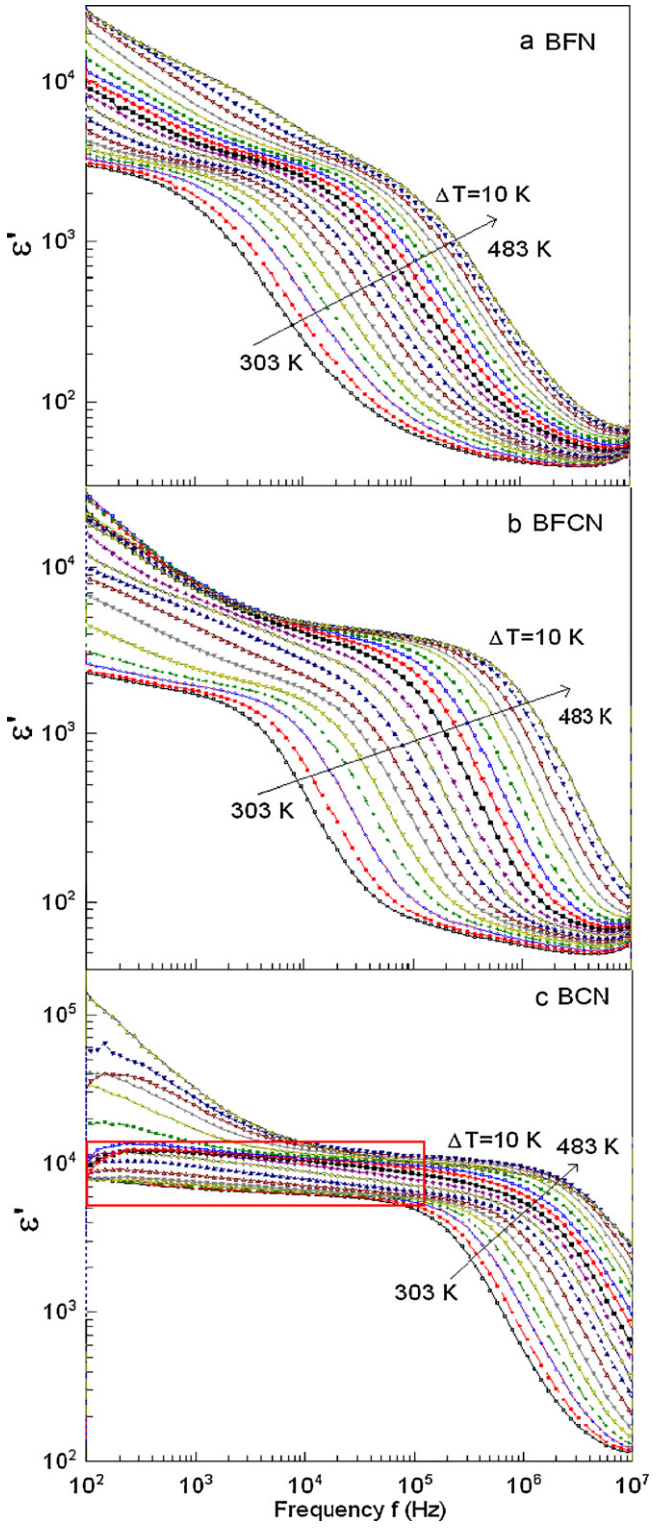

Fig. 3. The frequency response of the real part of the permittivity measured in the temperature range of 303–483 K for (a) BFN, (b) BFCN, and (c) BCN. In (c) for BCN, the constant value region is shown by the rectangular box.

It is revealed from Fig. 4 that the imaginary parts have no clear Debye peak and show monotonic variation with frequency. This nature of the relaxation peak indicates that in the low frequency region (<10^4 Hz), dipolar relaxation is masked by free charge relaxation [23]. It is to be noted here that the introduction of these free surface charges is an inevitable product of the high temperature sintering process [24,25]. In addition to the above, in ordered systems like the BCN, interaction between dipoles and induced charges at the local level, on replacement of Fe^{3+} ($3d^5$) by Co^{3+} ($3d^6$), may also affect the dielectric relaxation. The imaginary part of the permittivity (Fig. 4) is very high for each of these samples leading to higher values of electrical conductivity [26]. Furthermore, it is observed that $\varepsilon'(f)$ becomes nearly constant over a wide frequency and temperature range when Fe is completely replaced by Co (Fig. 3(c)).

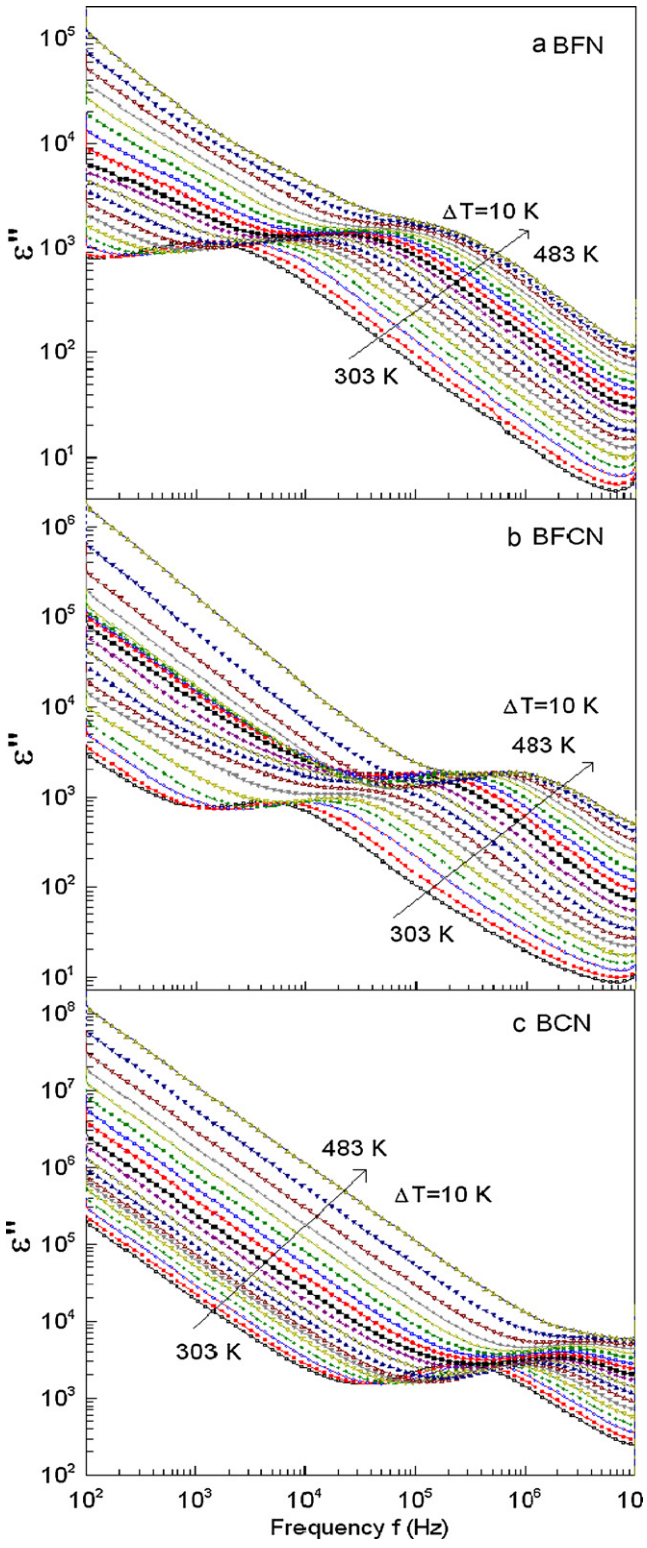

Fig. 4. The frequency response of the imaginary part of the permittivity measured in the temperature range of 303–483 K for: (a) BFN, (b) BFCN, and (c) BCN.

In the subsequent sections, we will investigate step by step the role of the intrinsic and/or extrinsic factors for the observed high dielectric constant. The complex permittivity analysis, the electrical modulus analysis, and the electrical conductivity analysis are applied as a tool for such an investigation.

3.3. Complex permittivity representation

It is observed that the complex permittivity data of our samples obey the Cole–Cole equation:

$$\varepsilon^* = \varepsilon' + i\varepsilon'' = \varepsilon_\infty + \frac{\Delta\varepsilon}{1+(i\omega\tau)^{1-\alpha}} - i\frac{\sigma_{dc}}{\varepsilon_0\omega}. \quad (1)$$

Here, τ is the mean relaxation time instead of the single relaxation time of pure Debye process while the Cole–Cole parameter α indicates the width of the relaxation time distribution and provides a measure of the poly-dispersive nature. The last term at the right-hand-side is due to the high conducting behaviour contributing only to the imaginary part [27], which is due to the displacement of charge carriers, rather than the effect of the polarization mechanism.

The fitting of the Cole–Cole equation was performed to study the dispersive and the conducting nature of the samples. It is seen from Fig. 5 that the observed non-zero values of the Cole–Cole parameter α indicate non-Debye type poly-dispersive nature of these samples. Similar deviation from Debye type relaxation in BFN was also recently observed through the Cole–Cole parameter analysis at high temperatures by Shanming et al. [13]. Further, constant values of α parameter (Fig. 5) for BFN and BFCN indicates that the distribution of the relaxation time is independent of temperature. In contrast to BFN and BFCN samples, a drastic increase in the α parameter for BCN above 370 K points at the enhanced interaction of the relaxing dipoles with the doped charge on replacement of Fe^{3+} ($3d^5$) by Co^{3+} ($3d^6$). The probable reason for the absence of such an interaction in the intermediate sample, BFCN, could be due to the enhancement in Co–Co distance in –Fe–Nb–Co–Nb–Fe– like chains in comparison to –Co–Nb–Co–Nb–Co– chains.

The temperature-dependent analysis of the relaxation time, τ, is a very useful tool to study such an interaction. It is seen that at ε''_{max} the product $\omega\tau$ becomes unity; hence the value of the relaxation time, τ, can be calculated using ω at ε''_{max}. But from the complex permittivity plot it is difficult to identify ε''_{max} values at $\varepsilon' = (\varepsilon_S + \varepsilon_\infty)/2$. The alternate and more accurate way to determine ε''_{max} value is to consider the relation [28]:

$$\varepsilon''_{max} = \frac{\varepsilon_S - \varepsilon_\infty}{2} \tan\left(\frac{(1-\alpha)\pi}{4}\right) \quad (2)$$

Using this relation, we have determined the mean relaxation time τ. In order to analyze explicitly the relaxation process, we have plotted the variation of the mean relaxation time τ against inverse temperature $1/T$ (Fig. 6(a)). The mean relaxation time is found to decrease with an increase in the Co concentration, sug-

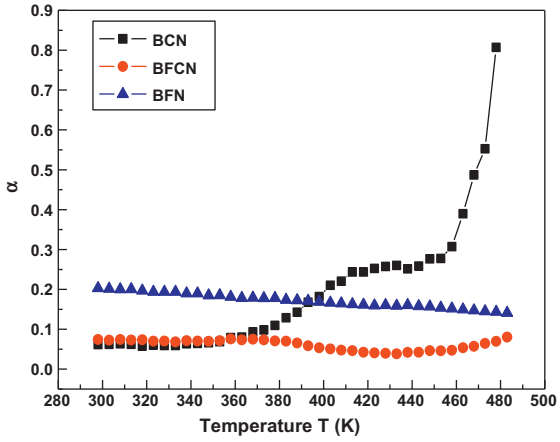

Fig. 5. The temperature-dependence of the Cole–Cole parameter, which indicates the width of the relaxation time distribution.

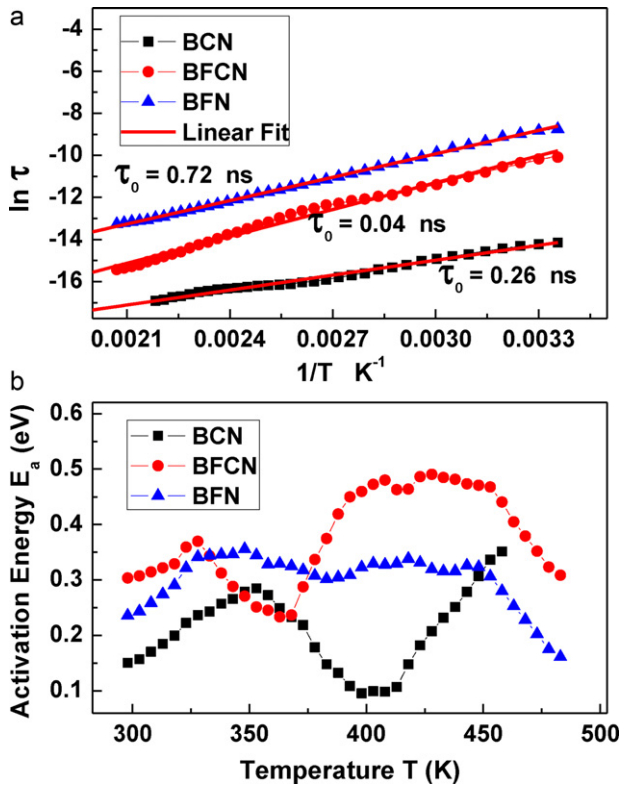

Fig. 6. (a) The Arrhenius plot fitting of the relaxation time and (b) the variation of the activation energy with temperature (using the Cole–Cole representation).

gesting an increase in the flexibility of charge carriers. The values of τ_0 obtained from the linear fits (Fig. 6(a)) are found to be in the range of 0.04–0.7 ns, which indicates the presence of non-dipole type relaxation in these distorted perovskite samples. In addition, non-linear curves of Fig. 6(a) show the deviation of the relaxation time from the Arrhenius law. The deviation from the Arrhenius law clearly suggests the temperature-dependent nature of the activation energy. The temperature-dependent value of the activation energy E_a can be calculated using [29]:

$$E_a = k\frac{d(\ln \tau)}{d(1/T)} \tag{3}$$

Here, k is the Boltzmann constant. The variation of the activation energy as a function of temperature is shown in Fig. 6(b). The activation energies (E_a) predominantly lie between 0.1 eV and 0.35 eV, which is very close to the activation energy of the singly ionized oxygen vacancies (0.1 eV) [24]. This clearly suggests that the observed dielectric relaxation is due to the interaction of free surface charges with singly ionized oxygen vacancies. The observed less activation energy for BCN in comparison with BFN (Fig. 6(b)) could be due to the doped electrons of Co^{3+} ($3d^6$): relaxation through free doped charges in BCN requires less activation energy in comparison with the relaxation through induced space charge due to oxygen vacancies in BFN. In contrast to this, the observed unusually higher activation energy values in BFCN therefore may be due to co-existence of micro domains of BFN and BCN within the grains. As suggested before, this might result in distortion of long-range order of –Fe–Nb–Fe– or –Co–Nb–Co– chains.

In order to confirm the relaxation parameters, we have carried out a similar analysis using $\varepsilon''(f)$ curves shown in Fig. 4. The nature of relaxation time obtained using $\varepsilon''(f)$ curves is found to be consistent with Cole–Cole analysis. The values of the activation energy, E_a, and the mean relaxation time, τ_0, hence indicate that the intrinsic contribution of chemical substitution as well as interaction of free space charges with dipoles collectively leads to giant dielectric constants (>10^4) in 1:1 type relaxors.

3.4. Electrical modulus representation

The space charge–dipole interaction can be probed effectively through the electrical modulus formalism as it overcomes contribution of high electrical conductivity appropriately [23,27,30]. The complex electric modulus $M^*(\omega)$ is defined as the inverse of the complex permittivity $\varepsilon^*(\omega)$:

$$M^* = \frac{1}{\varepsilon^*} = M' + iM'' \tag{4}$$

Here, real part of the electric modulus

$$M' = \frac{\varepsilon'}{\varepsilon'^2 + \varepsilon''^2} \tag{5}$$

and the imaginary part of electric modulus

$$M'' = \frac{-\varepsilon''}{\varepsilon'^2 + \varepsilon''^2} \tag{6}$$

Figs. 7 and 8 show the frequency responses of the real and the imaginary parts of the electric modulus with the variation of temperature. In Fig. 8, two distinct relaxations are observed for each sample. The nature of the first low frequency relaxation (<10^5 Hz) peak is non-Debye type indicating domination of free charge carriers. On the other hand, the second relaxation peak (>10^5 Hz) is due to the presence of the Debye type dipole relaxation. Here, as a matter of convenience, we have analyzed only the low frequency relaxation, as it helps in understanding the origin of the high dielectric constant.

The mean relaxation time is calculated by equating $\omega\tau$ to unity at the peak value of $M''(f)$. The non-linear nature of curves in Fig. 9 indicates that the Arrhenius law of relaxation is not obeyed by the relaxation time. Therefore, the activation energy of relaxation, E_a, is calculated using the derivative Eq. (3). The variation of the activation energy as a function of the inverse temperature is shown in Fig. 9(b). The activation energy for BFN is found to be nearly constant ($E_a \sim 0.4$ eV) in agreement with the complex permittivity representation, whereas in BCN, the E_a values increases gradually from 0.2 eV to 1.4 eV for the same temperature range. A systematic enhancement of the activation energy for temperatures greater than 450 K, suggests the development of doubly ionized oxygen vacancies. The observed E_a values in the range of 0.1–0.3 eV and then its gradual movement towards >0.6 eV indicate the increased interaction of space charge with singly/doubly ionized oxygen vacancies in Co rich samples. Such an interaction of space charge with the oxygen vacancies was masked by conduction of doped charges in the complex permittivity representation.

3.5. Electrical conductivity analysis

The analysis of charge-induced dielectric relaxation as a function of Co doping at Fe site requires a detailed investigation of the conduction mechanism. The real part of the conductivity data, σ', as a function of frequency and temperature is shown in Fig. 10. It exhibits three different conductivity regions in these samples: (1) low-frequency plateau, (2) mid-frequency dispersion and (3) high-frequency plateau. The low-frequency plateau is related to the dc conductivity originating from the free charge carriers. It is emphasized that instead of the low-frequency plateau here we have observed low-frequency dispersion (LFD) for BFN sample, indicating an apparent ac conductivity contribution even in low-frequency region. This may be due to the absence of free charges required for dc conduction in BFN. The overall observed values of the dc conductivity are very high ($\sim 10^{-5}\ \Omega^{-1}\ cm^{-1}$ or more). Comparison of

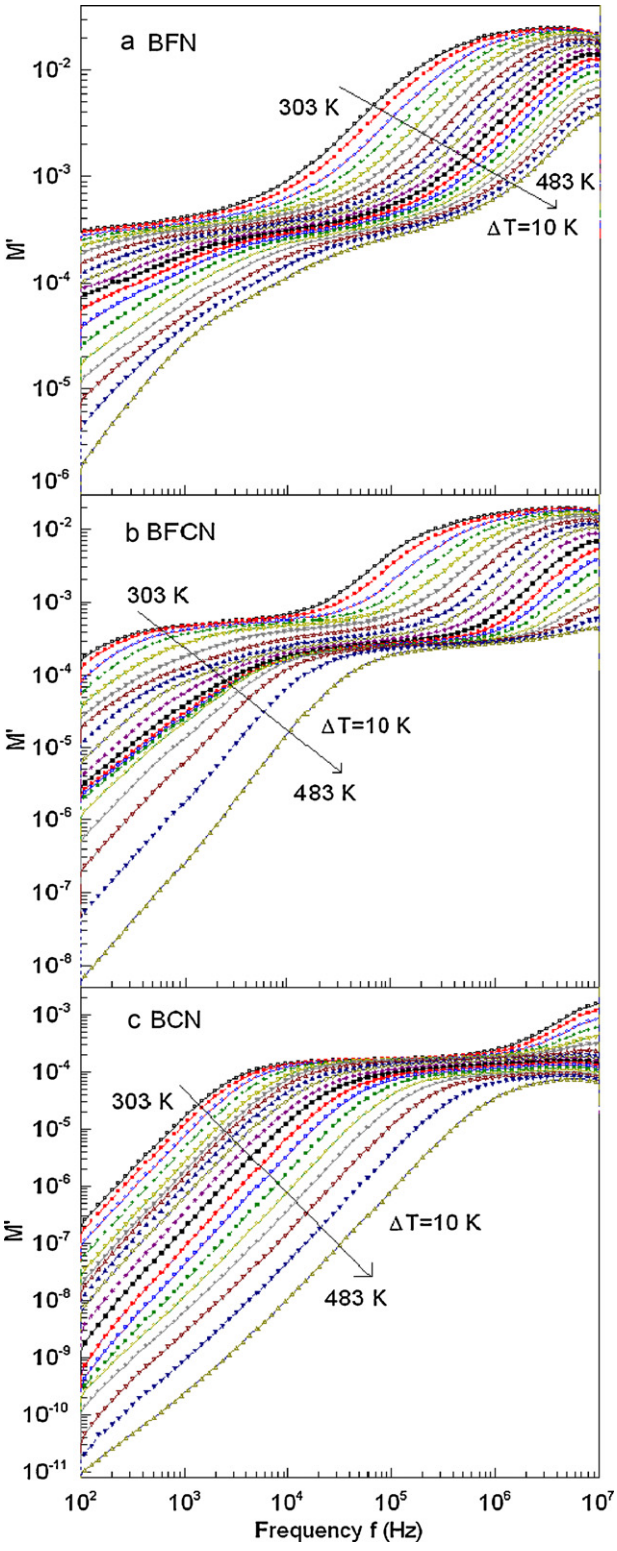

Fig. 7. The frequency response of the real part of the electric modulus measured in the temperature range of 303–483 K for: (a) BFN, (b) BFCN, and (c) BCN.

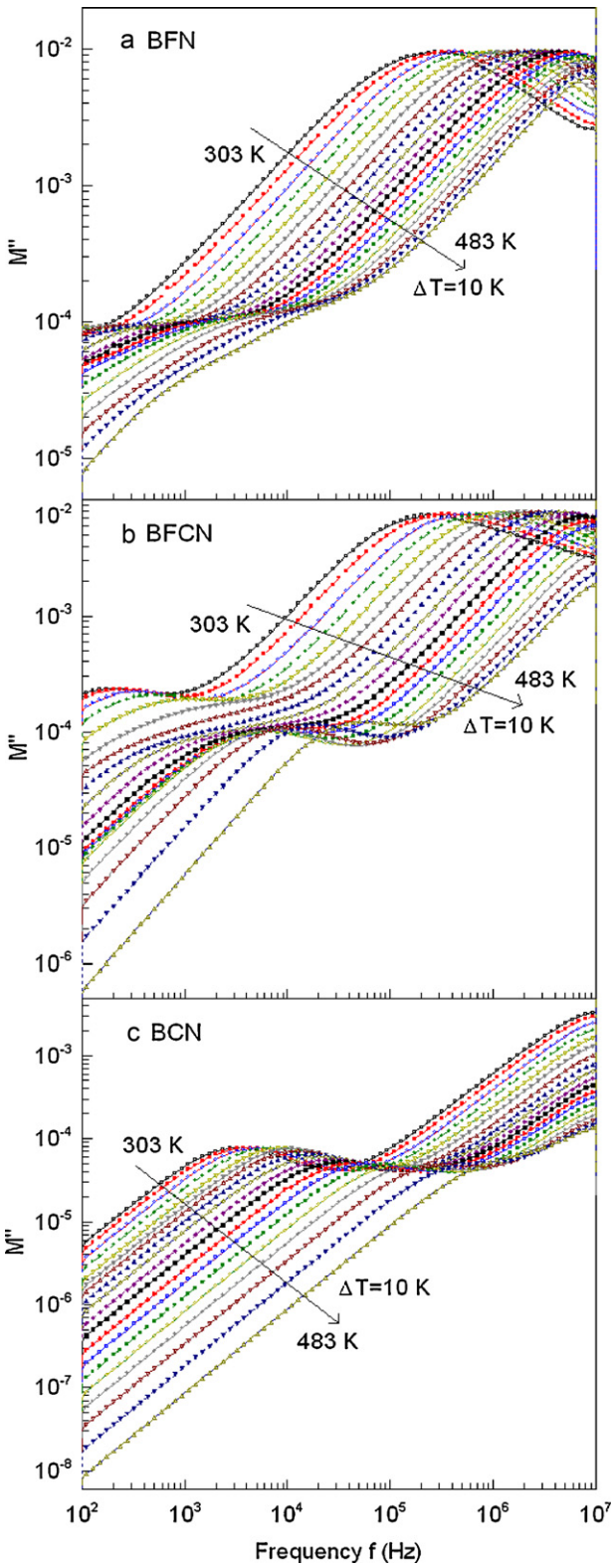

Fig. 8. The frequency response of the imaginary part of the electric modulus measured in the temperature range of 303–483 K for: (a) BFN, (b) BFCN, and (c) BCN.

the absolute values of the dc conductivity data shows an increase in the conductivity as Fe is replaced by Co. This clearly suggests that, for the Fe rich samples low-frequency conduction is predominantly due to oxygen vacancy induced electrons, while for the Co rich samples additional contribution comes from the movement of the doped electrons originating from the substitution of Fe^{3+} ($3d^5$) by Co^{3+} ($3d^6$). Doped electron produces conductivity due to the back and forth movement between Co and O. Therefore, the rapid increase in the conductivity values of Co rich samples is predominantly originating from the electron doping (intrinsic factor) rather than contributions from the oxygen vacancy (extrinsic factor) related conduction. This is further supported by the fact that the likely concentrations of oxygen vacancy will always be less than the

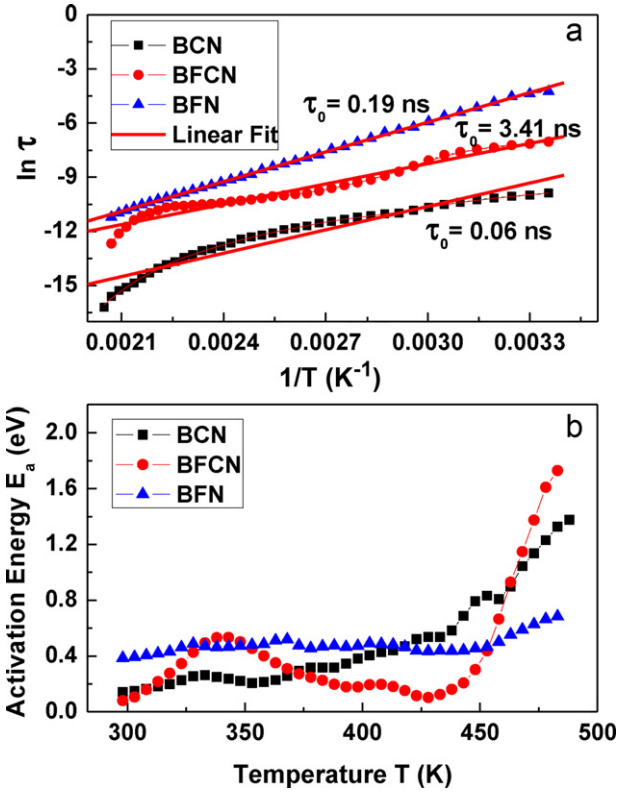

Fig. 9. (a) The Arrhenius plot fitting of the relaxation time and (b) the variation of the activation energy with temperature (using the $M''(f)$ representation).

concentration of Co^{3+} ($3d^6$) in the micro domain. It is to be noted here that attempts have been made by others to reduce oxygen vacancy induced conductivity losses through columbite method and microwave synthesis [13,31].

The observed strong dispersion at mid-frequency and the plateau at the high frequency are related to the ac conductivity. In order to comprehensively understand the behaviour of the conduction process, data were analyzed using the modified power law [32] of the ac conduction, Eq. (7):

$$\sigma' = \sigma_0\omega^{S_0} + \sigma_{ac_1}\omega^{S_1} + \sigma_{ac_2}\omega^{S_2} = \sigma_{dc} + \sigma_{ac_1}\omega^{S_1} + \sigma_{ac_2}\omega^{S_2} \quad (7)$$

The first term on the right-hand-side of Eq. (7) indicates the dc conductivity ($s = s_0 = 0$) as observed in the low-frequency region. The second and third terms represent the mid-frequency 'strong' dispersion ($s = s_1$) and the high-frequency 'weak' dispersion (plateau $s = s_2 \approx 0$), respectively. The values of the s parameter are obtained using the derivative equation:

$$s = \frac{d\ln\sigma'}{d\ln\omega} \quad (8)$$

Fig. 11 shows the frequency dependence of the s parameter at room temperature. As pointed out earlier, a not so distinct relaxation peak in ε'' vs. f curve (Fig. 4) as well as in M'' vs. f curve (Fig. 8), is now clearly resolved in the form of a peak in s vs. $\ln\omega$ curve (Fig. 11). Here the non-zero values of the s_0 parameter for BFN sample at low frequencies are due to the low-frequency dispersion (LFD). In the mid-frequency region, the s parameter increases rapidly and after showing a peak, it becomes nearly linear at higher frequencies. The values of the s_1 parameter at peaks are found to be greater than unity while the values of the s_2 parameter are close to zero. It is noted that generally the values of the frequency exponent s lie $0 \le s \le 1$ and the peak appears in GHz region for various ceramic oxides [33–35], but we have observed it in the MHz region.

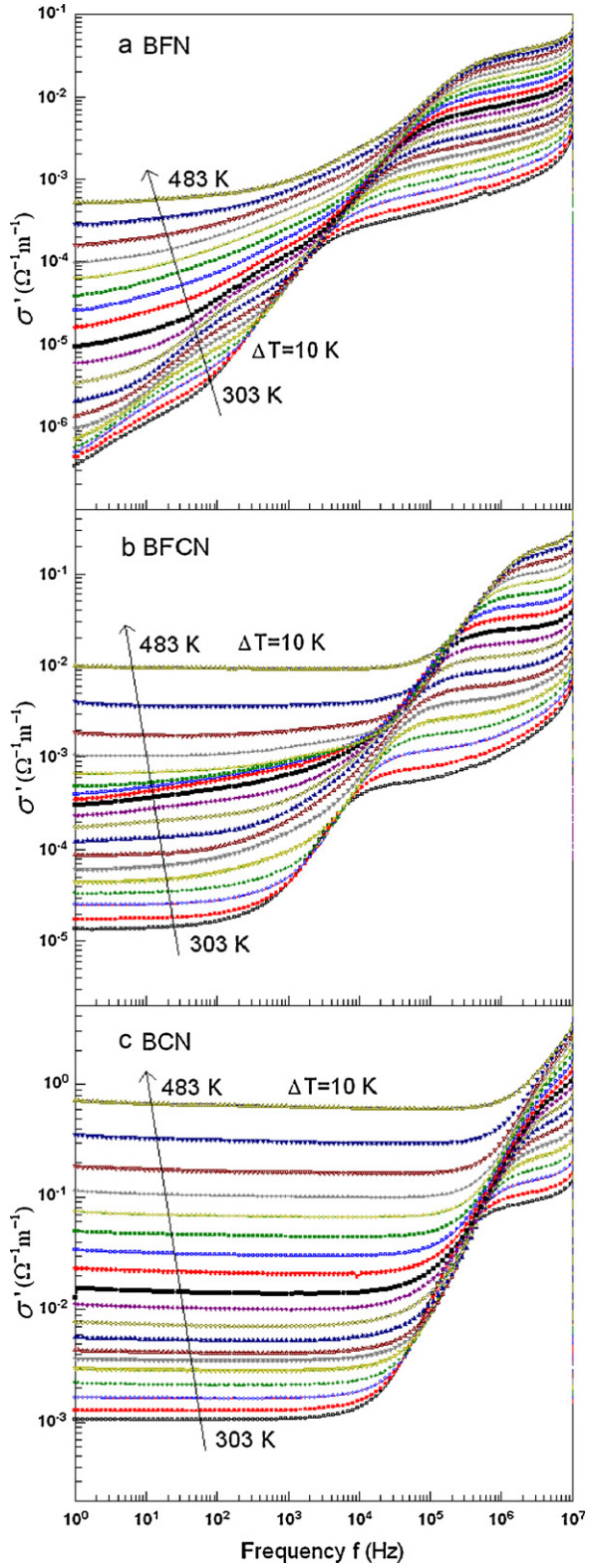

Fig. 10. The frequency response of the real part of the complex conductivity for (a) BFN, (b) BFCN, and (c) BCN at different temperatures ranges from 298 K to 483 K with an interval of 5 K.

The observed nature of s in various frequency regions can be explained using the JRM of Funke [36,37], who successfully used it to explain the hopping of ions. In the present case, we have used the same model to explain the hopping of the induced dipoles for the entire s vs. $\ln\omega$ region. It is inferred from the JRM that the

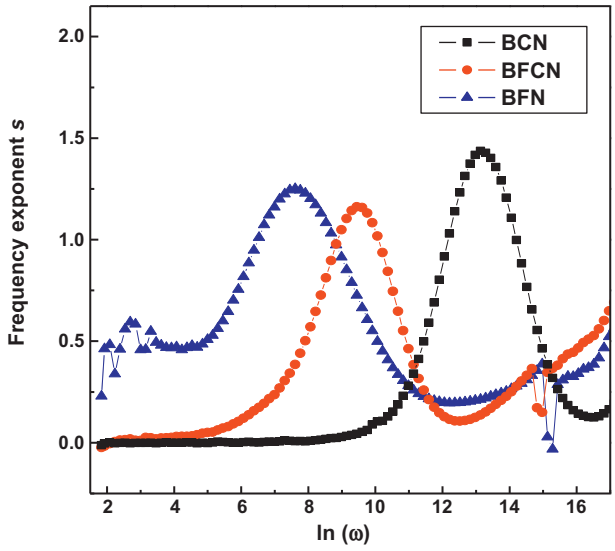

Fig. 11. The room temperature values of the frequency exponent s as a function of the frequency, obtained using the derivative curves.

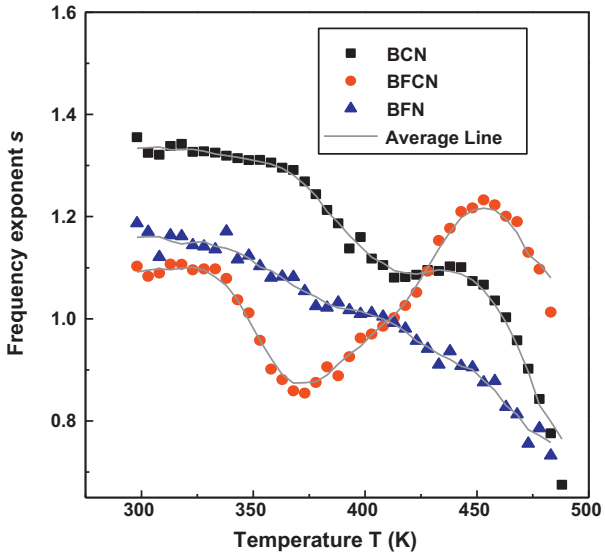

Fig. 12. The peak values of the frequency exponent s vs. the absolute temperature T.

constant values of s_0, related to the low-frequency region, results from the long-range translational motion of the conduction carriers (i.e., induced electrons). Here any attempt (by the dipoles) to conduct through the hopping mechanism becomes unsuccessful. As the input ac frequency increases, the rate of successful hopping, indicated by the frequency exponent s, increases. The conductivity in this region corresponds to the short-range translational hopping related to forward–backward jump. The peak position represents a condition where the number of successful and unsuccessful attempts becomes nearly equal. Beyond this region, the number of carriers (dipoles/oxygen vacancies) available for hopping gradually reaches saturation. This results in a reduction of the frequency exponent 's'. The high-frequency plateau, indicated as s_2, corresponds to a saturation region of charge carriers undergoing relaxational hopping. The shifting of the peak position towards high frequencies in the curves between s vs. ln ω is due to the gradual increase of the hopping-length with the gradual increase in cell dimensions resulting from the gradual replacement of Fe by Co. In this way, through the Jump Relaxation Model we have successfully filtered the contribution of the free doped charges, induced space charges, and the oxygen vacancy induced dipoles in the entire measured frequency range.

The temperature dependence of the s parameter for the critical mid-frequency region is shown in Fig. 12. It shows a nonlinear nature of the frequency exponent with temperature. According to the correlated barrier hopping (CBH) model [38,39], the parameter s has the form:

$$s = 1 - \frac{6kT}{[W_M - kT\ \ln(1/\omega\tau_0)]}, \tag{9}$$

Here, W_M is the energy required to cross the barrier height. The model predicts downward nature of s parameter for small values of W_M/kT. On the other hand, the increasing nature of s at high temperatures can be explained using the small polaron tunneling (SPT) [38,39] model given by:

$$s = 1 - \frac{4}{\ln(1/\omega\tau_0) - W_H/kT}, \tag{10}$$

Here, W_H is the activation energy required for polaron transfer. Small polarons are generally assumed to be so localized that their distortion clouds do not overlap. Therefore, the ac conductivity only in the high temperature limit is expected to be due to tunneling of randomly distributed carriers trapped at structural defects [38].

Nearly identical downward variation of the frequency exponent s for BFN and BCN samples indicates that the conduction process is predominantly due to the correlated barrier hopping (CBH) of electrons. In the intermediate sample BFCN, up to 370 K, CBH mechanism is dominating, but above this temperature (370–450 K), due to disruption of long-range lattice order, as pointed out earlier, the contribution of localized electron induced small polaron tunneling appears to be involved in the conduction process.

4. Conclusion

Here we have shown that the origin of the high dielectric constant in the cubic 1:1 type $Ba[(Fe_{1-x}Co_x)_{1/2}Nb_{1/2}]O_3$ compound is predominantly due to the interaction of the induced dipoles with the space charges. The suitable iso-valent substitution-induced softening of dipolar oscillations as well as electron doping due to substitution of Fe by Co enhances the above interaction. This, in turn, significantly upgrades the values of the dielectric constant to giant levels (>10^4 times) with a wide operational range of frequency and temperature.

The crucial conduction mechanism study in $Ba[(Fe_{1-x}Co_x)_{1/2}Nb_{1/2}]O_3$ samples shows that the dc conductivity contribution originates in different proportions from the oxygen vacancy induced free charges as well as from the introduction of doped electrons owing to the substitution of Fe^{3+} ($3d^5$) by Co^{3+} ($3d^6$). Present analysis of the frequency exponent s based on the Jump Relaxation Model completely bifurcates the conductivity response originating from (1) the free doped charges, (2) the induced space charges, and (3) the oxygen vacancy induced dipoles in the entire measured frequency range. The nonlinear nature of the ac conductivity mainly obeys the hopping mechanism but in intermediate composition (BFCN), the conduction process also involves a significant polaron tunneling. The temperature, as well as distortions along intra grain length of –Nb–Fe/Co–Nb– chains, decides the percentage contribution of polaron tunneling and/or correlated barrier hopping to the conductivity.

Acknowledgements

Authors are thankful to UGC-DAE-CSR, Indore centre for providing financial support and measurement facilities. We are also

thankful to UGC-DRS program for providing XRD and impedance measurement facility at our department.

References

[1] G.H. Haertling, J. Am. Ceram. Soc. 82 (1999) 797–818.
[2] K. Uchino, Ferroelectrics 151 (1994) 321–330.
[3] J.T. Wang, C. Zhang, Ferroelectrics 301 (2004) 211–214.
[4] W.Z. Zhu, A. Kholkin, P.Q. Mantas, J.L. Baptista, J. Eur. Ceram. Soc. 20 (2000) 2029–2034.
[5] L.E. Cross, Ferroelectrics 76 (1987) 241–267.
[6] F. Yuan, Z. Peng, J.-M. Liu, Mater. Sci. Eng. B 117 (2005) 265–270.
[7] S. Saha, T.P. Sinha, J. Phys. Condens. Matter 14 (2002) 249–258.
[8] S. Saha, T.P. Sinha, Phys. Rev. B 65 (2002) 134103–134109.
[9] S. Ke, H. Huang, H. Fan, Appl. Phys. Lett. 89 (2006) 182904–182906.
[10] J. Liu, Chun-Gang Duan, Wei-Guo Yin, W.N. Mei, R.W. Smith, J.R. Hardy, Phys. Rev. B 70 (2004) 144106-1–144106-7.
[11] S. Eitssayeam, U. Intatha, K. Pengpat, G. Rujijanagul, K.J.D. MacKenzie, T. Tunkasiri, Curr. Appl. Phys. 9 (2009) 993–996.
[12] F. Zhao, Z. Yue, J. Pei, D. Yang, Z. Gui, L. Li, Appl. Phys. Lett. 91 (2007) 052903-1–052903-3.
[13] S. Ke, H. Huang, H. Fan, H.L.W. Chan, L.M. Zhou, Ceram. Int. 34 (2008) 1059–1062.
[14] I.P. Raevski, S.A. Prosandeev, A.S. Bogatin, M.A. Malitskaya, L. Jastrabik, J. Appl. Phys. 93 (2003) 4130–4136.
[15] Z. Wang, X.M. Chen, L. Ni, X.Q. Liu, Appl. Phys. Lett. 90 (2007) 022904-1–022904-3.
[16] Y.Y. Liu, X.M. Chen, X.Q. Liu, L. Li, Appl. Phys. Lett. 90 (2007) 192905-1–192905-3.
[17] Z. Abdelkafi, N. Abdelmoula, H. Khemakhem, O. Bidault, M. Maglione, J. Appl. Phys. 100 (2006) 114111-1–114111-6.
[18] C. Elissalde, J. Ravez, J. Mater. Chem. 11 (2001) 1957–1967.
[19] D.C. Sinclair, T.B. Adams, F.D. Morrison, A.R. West, Appl. Phys. Lett. 80 (2002) 2153–2155.
[20] M.C. Ferrarelli, T.B. Adams, A. Feteira, D.C. Sinclair, A.R. West, Appl. Phys. Lett. 89 (2006) 212904-1–212904-3.
[21] J.D. Lee, Concise Inorganic Chemistry, fifth edition, second Indian reprint, Blackwell Science Asia Pty Ltd., Victoria 3053, Australia, 2006.
[22] Chung-Hsin Lu, Chi-Yuan Hu, Chung-Hsien Wu, Mater. Lett. 61 (18) (2007) 3959–3962.
[23] A. Molak, M. Paluch, S. Pawlus, J. Klimontko, Z. Ujma, I. Gruszka, J. Phys. D: Appl. Phys. 38 (2005) 1450–1460.
[24] C. Ang, Z. Yu, L.E. Cross, Phys. Rev. B 62 (2000) 228–236.
[25] S. Bu, E. Shin, G. Park, Appl. Phys. Lett. 73 (1998) 1442–1444.
[26] R.H. Cole, J. Chem. Phys. 23 (1955) 493–499.
[27] K.C. Kao, Dielectric Phenomena in Solids, Elsevier Academic Press, USA, 2004.
[28] K.S. Cole, R.H. Cole, J. Chem. Phys. 9 (1941) 341–351.
[29] J. Jadżyn, D. Baumen, J.-L. Déjardin, M. Ginovska, G. Czechowski, Acta Phys. Pol. A 108 (2005) 479–489.
[30] F.A. Grant, J. Appl. Phys. 29 (1958) 76–81.
[31] N. Charoenthai, R. Traiphol, G. Rujijanagul, Mater. Lett. 62 (2008) 4446–4448.
[32] J.P. Tiwari, K. Shahi, Philos. Mag. 87 (2007) 4475–4500.
[33] S. Mahboob, G. Prasad, G.S. Kumar, J. Mater. Sci. 42 (2007) 10275–10283.
[34] S. Mollah, K.K. Som, S. Chakraborty, A.K. Bera, S. Chatterjee, S. Banerjee, B.K. Chaudhuri, Phys. Rev. B 51 (1995) 17512–17520.
[35] N. Ortega, A. Kumar, P. Bhattacharya, S.B. Majumder, R.S. Katiyar, Phys. Rev. B 77 (2008) 014111-1–014111-10.
[36] K. Funke, Prog. Solid St. Chem. 22 (1993) 111–195.
[37] K. Funke, J. Non-Crystalline Solids 172–174 (1994) 1215–1221.
[38] S.R. Elliott, Adv. Phys. 36 (1987) 135–217.
[39] R. Gangopadhyay, A. De, S. Das, J. Appl. Phys. 87 (2000) 2363–2372.